Soft Matter

Cuboidal liquid crystal phases under multiaxial geometrical frustration

Journal:	*Soft Matter*
Manuscript ID	SM-ART-10-2019-002021.R1
Article Type:	Paper
Date Submitted by the Author:	18-Nov-2019
Complete List of Authors:	Palacio Betancur, Viviana; University of Chicago, Pritzker School of Molecular Engineering Armas-Pérez, Julio C; University of Chicago, Institute for Molecular Engineering; Universidad de Guanajuato, División de Ciencias e Ingenierías Villada-Gil, Stiven; Universidad Nacional de Colombia Sede Medellin, Departamento de Materiales y Minerales; Politecnico Colombiano Jaime Isaza Cadavid, Facultad de Ciencias Basicas, Sociales y Humanas Abbott, Nicholas; Cornell University, Hernandez-Ortiz, Juan; Universidad Nacional de Colombia, Sede Medellinin, Department of Materials and Nanotechnology; University of Chicago, Institute for Molecular Engineering de Pablo, Juan; Liew Family Professor of Molecular Theory and Simulation, Institute for Molecular Engineering

SCHOLARONE™
Manuscripts

Soft Matter

Cuboidal liquid crystal phases under multiaxial geometrical frustration[†]

Viviana Palacio–Betancur,[a] Julio C. Armas–Pérez,[b] Stiven Villada–Gil,[c,d] Nicholas L. Abbott,[e] Juan P. Hernández–Ortiz,[a,c‡] and Juan J. de Pablo[a,f*]

Cuboidal liquid crystal phases - the so-called blue phases - consist of a network of topological defects arranged into a cubic symmetry. They exhibit striking optical properties, including Bragg reflection in the visible range and fast response times. Confining surfaces can interfere with the packing of such a network, leading to structures that have not been explored before. In this work, a Landau–de Gennes free energy formalism for the tensor alignment field $\mathbf{Q}$ is used to investigate the behavior of chiral liquid crystals under non-isotropic confinement. The underlying free energy functional is solved by relying on a Monte Carlo method that facilitates efficient exploration of configuration space. The results of simulations are expressed in terms of phase diagrams as a function of chirality and temperature for three families of spheroids: oblate, spherical, and prolate. Upon deformation, blue phases adapt and transform to accommodate the geometrical constraints, thereby resulting in a wider range of thermal stability. For oblate spheroids, confinement interferes with the development of a full blue phase structure, resulting on a combination of half skyrmions. For prolate spheroids, the blue phases are hybridized and exhibit features of blue phases I and II. More generally, it is shown that mechanical deformation provides an effective means to control, manipulate and stabilize blue phases and cholesterics confined in tactoids.

1 Introduction

Blue phases arise spontaneously in chiral liquid crystals. they consist of networks of defect lines that organize themselves into space filling lattices with cubic symmetry[1]. Technological applications include low–energy consumption displays[2], optical sensors[3–5], and photonic crystals[6–9]. Blue phases (BPs) have attracted attention for their fast response to external stimuli[10,11], but their narrow range of thermal stability poses challenges to their use. Past efforts to stabilize BPs have focused on addition of dopants

[a] *Pritzker School of Molecular Engineering, University of Chicago, Chicago, IL 60637, USA.*

[b] *División de Ciencias e Ingenierías, Campus León, Universidad de Guanajuato, Loma del Bosque 103, León (Gto.) 37150, México*

[c] *Departamento de Materiales y Minerales, Universidad Nacional de Colombia–Sede Medellín, Medellín, Colombia.*

[d] *Facultad de Ciencias Básicas, Sociales y Humanas. Politécnico Colombiano Jaime Isaza Cadavid. Medellín, Colombia.*
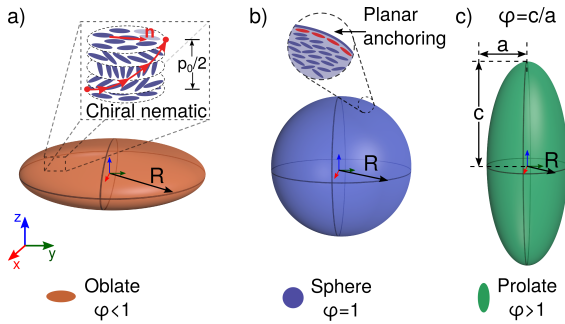
[e] *Department of Chemical and Biomolecular Engineering, Cornell University, Ithaca, NY, USA.*

[f] *Materials Science Division, Argonne National Laboratory, Lemont, IL 60439, USA. Corresponding authors:* ‡*E-mail: jphernandezo@unal.edu.co*

*E-mail: depablo@uchicago.edu.

to nematic phases[12–19], and little work has been devoted to the study of geometrical confinement as a means to manipulate their structure.

Geometrical frustration can be used to generate new families of defect configurations. More specifically, one can engineer the balance between the surface and elastic contributions to the free energy[20], and favor anchoring driven transitions over bulk morphologies. For instance, cholesteric liquid crystals (ChLCs) confined in channels form structures similar to skyrmions[21–24], and the orientation of the cholesteric can be changed through surface functionalization[25–27]. Under spherical confinement, BPs reproduce their lattice order and may be manipulated to take advantage of the intrinsic topology of the chiral nematics to form knots or to braid nanoparticles[28–35].

A phase diagram for micron-sized droplets of chiral LCs has been reported previously by Martínez-González et al.[33]. In that work, the stability of each region was determined by minimizing the total free energy using a Ginzburg–Landau relaxation from initial *ansatze* configurations. A wide variety of configurations was reported, including twisted cylinders (TC), radial spherical structures (RSS), and blue phases one (BPI) and two (BPII). Some regions of the phase diagram correspond to the phases formed in bulk[36,37], and others do not.

Particle-based molecular simulations have shown that a freely

Fig. 1 Schematic of the types of tactoids. (a) Oblate, $\varphi < 1$. The insert shows an schematic of the behavior of a chiral nematic, where p_0 is the cholesteric pitch and $\mathbf{n}$ is the mean molecular orientation or director vector. (b) Sphere, $\varphi = 1$. The insert shows the planar alignment of the molecules at the surface. (c) Prolate, $\varphi > 1$. The aspect ratio φ is defined by the lengths c and a which are aligned with the Cartesian directions z and y. The cartoons next to each spheroid will be used throughout this paper to represent the geometry.

suspended LC droplet adopts a prolate geometry due to the elongated shape of the molecules [38]. The formation of non–spherical droplets has also been reported in lyotropic liquid crystals [39–42]. The anisotropy of these shapes induces chiral morphologies with a certain range of stability. For instance, mechanical deformation of a BPI has been used to tune optical response through an applied strain [43,44], providing options for the fabrication of low–voltage electro–optical devices. More recently, cellulose nanocrystal suspensions have been shown to form chiral nematic tactoids, which offer the possibility to reach greater lengths and higher aspect ratios, and can aid in separation processes for nanoparticles [45,46]. Building on these past studies, the central questions that we address here are whether it is possible to stabilize BPs by means of an external asymmetric physical constraint, as opposed to a chemical alteration, and whether the resulting phases undergo significant changes that may alter their optical properties.

A model chiral LC is confined into spheroids of different aspect ratios. We consider oblate, spherical, and prolate geometries. The reference geometry is a sphere with a radius of 500 nm; its axes are stretched to obtain isochoric geometries with different aspect ratios $\varphi = c/a$, where c and a are the lengths of the semi-principal axes aligned with the z and x Cartesian axes, respectively. An oblate is described by $\varphi < 1$, while a prolate is described by $\varphi > 1$. Accordingly, a sphere corresponds to $\varphi = 1$. Figure 1 shows the three type of spheroids and the orientation of the axes. The surface imposes a degenerate planar orientation on the LC material, and the pitch p_0 is defined in terms of N, which denotes the number of π–turns along the major axis. Note that for all geometries the cross section parallel to the xy-plane is a circle of radius R.

2 Thermodynamic model

The degree of positional and orientational order is described using a second-rank tensor order parameter defined by [47,48]:

$$\mathbf{Q}(\mathbf{x}, t) = \mathbf{M}_{\mathrm{II}}(\mathbf{x}, t) - \frac{\delta}{3}, \tag{1}$$

where δ is the 3×3 identity tensor and the second moment $\mathbf{M}_{\mathrm{II}}$ is obtained from the average molecular orientation $\mathbf{u}$ and the probability density of molecular orientations $\psi(\mathbf{u}, \mathbf{x}, t)$, i.e.

$$\mathbf{M}_{\mathrm{II}}(\mathbf{x}, t) = \int \mathbf{u}\mathbf{u}\psi(\mathbf{u}, \mathbf{x}, t)d\mathbf{u}. \tag{2}$$

The symmetric and traceless tensor order parameter may be written in terms of its eigenvalues and eigenvectors [49,50] as

$$\mathbf{Q} = S\left(\mathbf{n}\mathbf{n} - \frac{\delta}{3}\right) + \eta\left[\mathbf{n}'\mathbf{n}' - (\mathbf{n} \times \mathbf{n}')(\mathbf{n} \times \mathbf{n}')\right], \tag{3}$$

where $S(\mathbf{x})$ is the scalar order parameter related to the maximum eigenvalue, and the biaxiality $\eta(\mathbf{x})$ is connected to the other two eigenvalues. The order parameters are bounded by $S \in [-1/2, 1]$, and $\eta \in [-1/3(1 - S), 1/3(1 - S)]$. The eigenvectors, $\mathbf{n}$ and $\mathbf{n}'$, define an orthonormal basis $\{\mathbf{n}, \mathbf{n}', (\mathbf{n} \times \mathbf{n}')\}$ for the LC orientation.

The thermodynamic state is described in terms of a phenomenological free energy functional through the Landau–de Gennes formalism, that contains three contributions: a short–range Landau free energy f_L, which captures the isotropic–nematic transition, a long–range free energy that penalizes elastic distortions from an homogeneous state f_E, and a surface free energy that quantifies surface anchoring f_S. The free energy functional is defined in terms of $\mathbf{Q}$ as follows [47,48,51]:

$$F(\mathbf{Q}) = \int d^3\mathbf{x}[f_L(\mathbf{Q}) + f_E(\mathbf{Q}, \nabla\mathbf{Q})] + \oint d^2\mathbf{x}f_S(\mathbf{Q}). \tag{4}$$

The Landau density is expressed as a polynomial expansion of the tensor invariants. We use Doi's notation [47,52], which considers a unique scale for the energy:

$$f_L(\mathbf{Q}) = \frac{A}{2}\left(1 - \frac{U}{3}\right)\mathrm{tr}(\mathbf{Q}^2) - \frac{AU}{3}\mathrm{tr}(\mathbf{Q}^3) + \frac{AU}{4}\mathrm{tr}(\mathbf{Q}^2)^2, \tag{5}$$

where A and U are phenomenological coefficients that are material specific; with A the energy scale and U the parameter that controls the isotropic–nematic transition [47].

The elastic free energy density is modeled using Oseen–Frank's theory [53,54] and it is written in terms of the alignment tensor and its gradients [48,55],

$$f_E(\mathbf{Q}, \nabla\mathbf{Q}) = \frac{1}{2}L_1\frac{\partial Q_{ij}}{\partial x_k}\frac{\partial Q_{ij}}{\partial x_k} + \frac{1}{2}L_5\varepsilon_{ikl}Q_{ij}\frac{\partial Q_{lj}}{\partial x_k}, \tag{6}$$

where L_i are the elastic constants related to the different elastic moduli. For a uniaxial system these are defined by

$$L_1 = \frac{K}{2S^2}, \tag{7}$$

and

$$L_5 = \frac{2}{S^2}q_0K. \tag{8}$$

Where K is the elastic moduli. In this work we adopt the one–elastic constant approximation [48,51], in which all elastic deformations are penalized equally resulting in non-zero L_1 and L_5. L_5 quantifies the chirality of the LC with the inverse pitch $q_0 = 2\pi/p_0$, and ε_{ikl} is the Levi–Civita tensor.

The surface free energy density describes the interaction of the

liquid crystal with the confining surface; the condition for degenerate planar anchoring is imposed by the 4th order degenerate potential proposed by Fournier and Galatola[56]:

$$f_S(\mathbf{Q}) = \frac{W}{2}\left(\bar{\mathbf{Q}} - \bar{\mathbf{Q}}_\perp\right)^2 + \frac{W}{4}\left(\bar{\mathbf{Q}} : \bar{\mathbf{Q}} - S^2\right)^2, \qquad (9)$$

where $\bar{\mathbf{Q}} = \mathbf{Q} + S\delta/3$, $\bar{\mathbf{Q}}_\perp = \mathbf{p} \cdot \bar{\mathbf{Q}} \cdot \mathbf{p}$ is the tensor projection on the surface, and $\mathbf{p} = \delta - \nu\nu$.

The free energy functional is minimized using a theoretically-informed Monte Carlo (MC) relaxation method described in the literature[57–59]. During a MC simulation, Metropolis criteria are adopted to sample the free energy by proposing trial changes to the tensor order parameter $\mathbf{Q}$. In order to perform uniform sampling over its five independent components, $\mathbf{Q}$ is expressed in terms of an orthonormal tensor basis as presented by Hess et $al.$[60],

$$\mathbf{Q} = \sum_{v=1}^{5} a_v(\mathbf{x},t)\mathbf{T}^v, \qquad (10)$$

where the five scalar components a_v are projections of the tensor basis defined as follows:

$$\mathbf{T}^1 = \sqrt{3/2}\,[\mathbf{zz}]^{ST} = \sqrt{3/2}\left(\delta_{3i}\delta_{3j} - \delta_{ij}/3\right),$$

$$\mathbf{T}^2 = \sqrt{2}\,[\mathbf{xy}]^{ST} = \sqrt{2}\left(\delta_{1i}\delta_{2j} + \delta_{2i}\delta_{1j}\right)/2,$$

$$\mathbf{T}^3 = \sqrt{2}\,[\mathbf{xz}]^{ST} = \sqrt{2}\left(\delta_{1i}\delta_{3j} + \delta_{3i}\delta_{1j}\right)/2, \qquad (11)$$

$$\mathbf{T}^4 = \sqrt{1/2}\,(\mathbf{xx} - \mathbf{yy}) = \sqrt{1/2}\left(\delta_{1i}\delta_{1j} - \delta_{2i}\delta_{2j}\right),$$

$$\mathbf{T}^5 = \sqrt{2}\,[\mathbf{yz}]^{ST} = \sqrt{2}\left(\delta_{2i}\delta_{3j} + \delta_{3i}\delta_{2j}\right)/2,$$

where $[A]^{ST}$ is the symmetric and traceless projection operator, $\mathbf{x}$, $\mathbf{y}$, and $\mathbf{z}$ are the canonical $\mathfrak{R}^3$ basis, and δ_{ij} is the Kronecker delta.

The sequence of accepted trial moves forms a Markov chain of configurations, where each transition is accepted with a probability given by

$$P_{acc}(o \rightarrow n) = \min\left[1, \exp\left(-\beta\Delta F\right)\right], \qquad (12)$$

with $\beta^{-1} = k_B\hat{T}$ where k_B is the Boltzmann constant and $\hat{T}$ is an artificial temperature that we use for simulated annealing; ΔF is the change in the free energy after a trial move has been performed. For more information on the choice of $\hat{T}$, we refer the reader to previous work[57–59].

The numerical integration of the free energy functional is calculated with a Gauss–Legendre quadrature over a mesh of quadratic tetrahedral elements created with Cubit (version 14.1)[61] and optimized through libMesh[62]. The Finite Element mesh is able to capture the nuances of the geometries beyond the limits of traditional rectangular discretization techniques. This method has been proven to be versatile when studying intricate geometries and more complex systems [5,26,63,64], and it is consistent with other relaxation techniques[57–59,65].

3 Results

The chiral liquid crystal's nematic coherence length is $\xi_N = \sqrt{L_1/A} = 10$ nm; the elastic constant is $k_{11} = 16$ pN. The sur-

faces impose degenerate planar anchoring; we consider high ($W = 1 \times 10^{-3} J/m^2$), intermediate ($W = 1 \times 10^{-4} J/m^2$), and low ($W = 1 \times 10^{-5} J/m^2$) anchoring strengths. The chirality is controlled through the dimensionless parameter $N = 4R/p_0$, indicating the number of π–turns the director makes along a distance R. In order to build consistent phase diagrams for all geometries, we calculate the pitch necessary to keep N constant as φ varies. The phase diagrams are built in terms of the inverse reduced temperature $\tau = 9(3-U)/U$ and the chirality parameter N.

3.1 Free energy analysis

We begin by examining different contributions to the free energy functional as the aspect ratio is changed. We restrict this analysis to the strong anchoring conditions, $W = 1 \times 10^{-3} J/m^2$, and $U = 2.9$. Moderate and weak anchoring as well as lower temperatures follow similar trends. The consequences of changing W, U and N are reflected the phase diagrams, which are discussed in the following sections.

Figure 2 shows the total free energy as a function of the aspect ratio for different values of N. At first sight it appears that the free energy decreases monotonically as the aspect ratio increases; note, however, that as φ increases the chirality also increases. Recall that the chiral contribution to the free energy is negative, implying that the formation of defects stabilizes the system as L_5 increases. The behavior of the total free energy in Fig. 2 helps explain the effects of N: for $N < 2$ the dependence of the free energy on φ is less than when $N > 3$, and $N = 3$ serves to delineate different morphologies, where the strong decrease of the total free energy is accompanied by a change of the nature of the underlying defect structure.
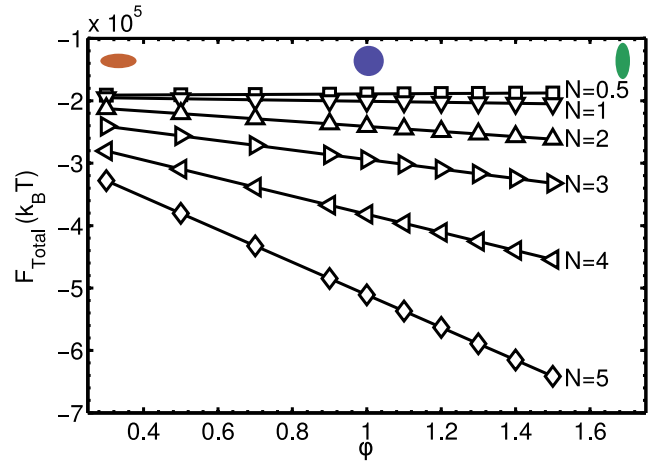
Fig. 2 Total free energy as a function of the aspect ratio, φ and different chiral systems distinguised by N. The free energy is calculated for strong anchoring conditions with $W = 1 \times 10^{-3} J/m^2$ and $U = 2.9$. The cartoons in the top of the figure indicate the type of spheroid.

Figures 3 and 4 show the different contributions to the free energy density as a function of φ for different values of N. According to Fig. 3, the Landau and surface free energy densities follow the same trend when the chirality and φ are modified. The monotonic behavior of these contributions as the chirality increases (purple arrow in Fig. 3) is a consequence of the forma-

tion of defects. Note that for all cases with $N < 2$, where the pitch values vary between 850 nm and 6 μm, these contributions are almost constant. Therefore, the system exhibits a nematic–like morphology, free of inner defects, or a cholesteric configuration, identified by the continuous twist of the director field; i.e. the distribution of the scalar order parameter in the bulk is uniform. For highly chiral systems, $N > 3$, the defect density increases dramatically and the local nematic order changes abruptly. The effect of φ (blue arrow in Fig. 3) translates into an increase in the tactoid axes along the z-direction, resulting in more space for nematic defects and increasing the Landau energy. The surface free energy penalties when $N < 2$ come from the surface boojums. For shorter pitches, the network of disclination lines is distributed throughout the bulk and touches the surface, forming a texture or patterns composed of various $\lambda^{-1/2}$ and λ^{+1} rotations of the director field, which are related to half skyrmions. The number of regions where there are surface penalties is therefore greater. The inset in Fig. 3 shows the surface area as a function of φ. Note that the surface area is minimized when $\varphi = 1$, and even though the oblate has the maximum surface area, it also exhibits larger patterns when compared to the prolate, contributing in a lesser manner to the energy penalties at the surface.
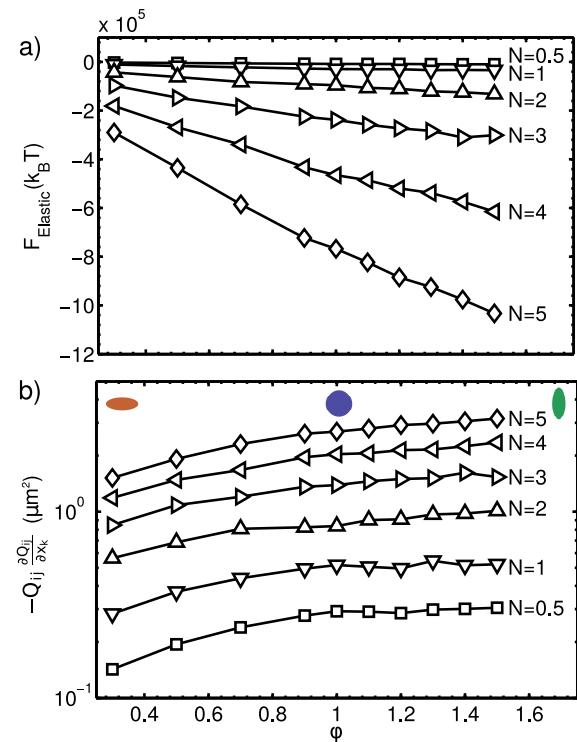
The total elastic free energy and the gradients of the chiral term are shown in Fig. 4. The decreasing character of this contribution is caused by the dominance of the chiral term, quantified by the elastic constant L_5. The elastic constant L_5 is proportional to the inverse pitch q_0, so smaller values of the pitch contribute to a decrease in the free energy by generating elastic deformations. The chiral term is therefore more dominant in prolates than oblates. Similar to the Landau and surface contributions, for high vales of N the distortions are stronger, resulting in higher contributions to the total free energy. In Fig. 4(Bottom) we show the contribution of the chiral elastic term normalized by the value of L_5, i.e. the effect of the pitch is removed. As φ increases these elastic gradients reach a plateau. Therefore, after removing the changing value of p_0, there is a specific aspect ratio, according to the value of N, where the contribution of the elastic free energy density does not change considerably. This behavior is an indication that freely suspended chiral droplets would not increase their aspect ratio indefinitely, and instead the final shape will be determined by the balance between elasticity and confinement, and additional contributions from the surface tension.

3.2 Phase diagrams

Three sets of diagrams are presented for $\varphi = 1$ (droplet), $\varphi > 1$ (prolate) and $\varphi < 1$ (oblate). The diagrams include strong anchoring conditions with $W = 1 \times 10^{-3} J/m^2$ and moderate with $W = 1 \times 10^{-4} J/m^2$. The morphologies for weaker anchoring strengths $W < 1 \times 10^{-4} J/m^2$ are similar to those for moderate conditions. As the geometry and anchoring are modified, some phases persist and others rearrange, leading to an expanded family of possible configurations. Figure 5 shows the phase diagram for a chiral LC in a spherical droplet as a function of τ and N. Strong anchoring conditions are used for Figure 5A, while moderate anchoring conditions are used for Fig. 5B. On the right of the
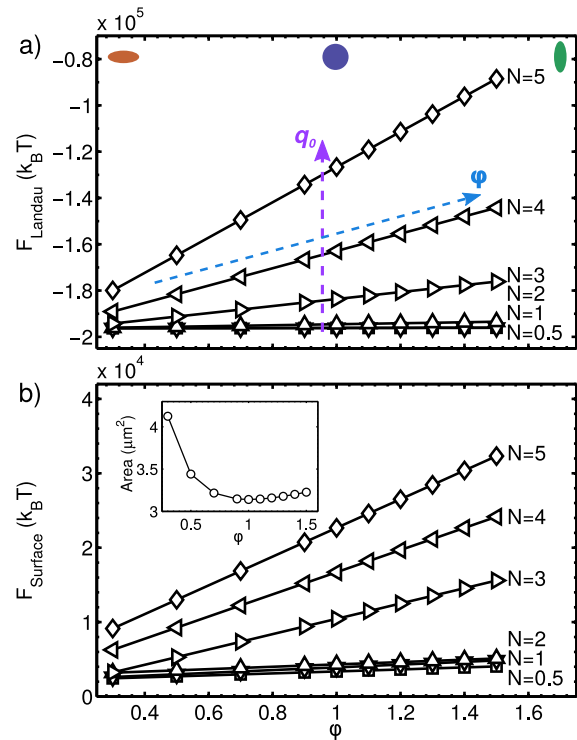
Fig. 3 (a) Landau and (b) surface free energy contributions as a function of the aspect ratio, φ, for different chiralities, N, under strong anchoring conditions, $W = 1 \times 10^{-3} J/m^2$, and $U = 2.9$. The cartoons on the top indicate the type of confining geometry. The arrows in (a) serve as guide for increasing aspect ratio (blue) and increasing q_0 (purple). The insert in (b) shows the surface area for the tactoids.

Fig. 4 (a) Elastic free energy and (b) chiral gradients as a function of the aspect ratio, φ, for different chiral system distinguished by N under strong anchoring $W = 1 \times 10^{-3} J/m^2$ and $U = 2.9$.

diagrams we depict the characteristic morphologies corresponding to each region.

One can observe two families of phases: one dictated by the surface ordering and the other governed by the bulk elasticity. When the surface dominates, Bipolar (B), Twisted Bipolar (TwBs), and Radial Spherical Structures (RSS) are observed. On the other hand, blue phases (BPI and BPII) are observed when the bulk dominates over the surface, thereby forming defect structures within the droplet. Surface anchoring and N serve as the control variables for the interplay between surface and bulk free energy contributions. Phase diagrams for blue phase droplets with strong anchoring conditions have been reported by Martínez-González *et al.* [33]. The morphologies presented there coincide with our results in figure 5A. Additionally, they introduce the idea of controlling and expanding the stability of the blue phase through spherical confinement and corroborated with experimental information. As we will show, this phenomena is not exclusive to droplets and in turn deforming the droplet results in interesting new features in the family of chiral tactoids.

For strong anchoring conditions, in the absence of chirality, the bipolar phase is observed with its two characteristic surface boojums. With increasing chirality, the boojums remain in the opposite poles as the director field twists inside the droplet following a helical pathway: this phase is the TwBs. As chirality increases at low temperature, the boojums approach each other in order to satisfy the high induced twist of the director field. They are not located in opposite poles and eventually merge to form one single surface defect, which ties a knot defect similar to the Frank-Prize structure. This phase is the RSS.

For high chirality and temperature ($\tau > 0$), the LC morphologies are characterized by a network of disclination lines. These are the BPs. For non-confined systems, the defect networks form cubic lattices (BPII with a O_2 symmetry and BPI with O_8 symmetry). For confined systems, the periodicity of the BP structures is interrupted, and the defect lines bend and deform to conform with the geometry. We identify the BPII when the defect lines merge in the center of the cell (blue highlights in the red morphologies in Fig. 5). On the other hand, the BPI defect network is such that they don't interact with each other (green defect lines in Fig. 5). For the rest of the manuscript, BPII is shown in red and blue colors, while the BPI is colored in green. Although the BP defects are highly bent, the surface structure forms a regular hexagonal pattern with penta–hepta defects composed of an array of $\lambda^{-1/2}$ and λ^{+1} disclinations. These surface structures are typical of cholesteric phases where there is no abrupt change in the molecular orientations. The pattern is better defined for a narrow interval of temperatures that coincide with the stability region of the BPII. At lower temperatures, more regions obey the planar anchoring conditions, thereby narrowing the surface pattern and presenting more red regions, where molecules satisfy the planar anchoring conditions.

For moderate and weak anchoring conditions (Fig. 5B), the surface-dominated morphologies are only found in the low chirality regime. For non-chiral systems, the bipolar phase transforms into a Uniaxial (U) phase, where the two surface boojums no longer exist. At low chirality, the director field twists and forms

a Twisted Cylinder (TC) structure. The TC morphology can be interpreted as a stack of layers, each with a λ^{+1} disclination, which is discussed in more detail later on. For intermediate chirality ($N = 2, 3$), the resulting phases are precursors of fully developed BPs. At low temperatures, we find a τ–Cholesteric phase (τ-Ch) that exhibits a single $\tau^{-1/2}$ defect across the bulk and a trefoil pattern on the surface. On the other hand, at higher temperatures, defects across the bulk become unstable, leading to formation of two u-shaped defects in what we call a pre-BPI morphology. The location and orientation of these line defects are similar to a defective joint on a BPII; however, the pitch values and temperature range of this morphology are more fitting of a BPI. At high chirality we encounter BPs. While the stability region for the BPII is not altered, once the anchoring is decreased, the BPI is now stable for a wider interval of temperatures and chiralities. The regular periodic structure in the bulk is only found at temperatures near the isotropic transition. The defect lines at low temperatures show a propensity to form tangles and knotts, thus creating highly deformed lattice cells.

The prolate is formed by "pulling" two opposite poles of the droplet. The surface area and curvature are changed and the boundaries within the droplet phase diagram move according to the value of φ. The prolate phase diagrams are shown in Fig. 6 for $1.1 < \varphi < 1.5$. As a general trend, the morphologies are similar to those from Fig. 5.

For strong anchoring conditions, Fig. 6A, the BPI phase is stabilized and the regions for the TwBS and the RSS phases shrink as φ increases. For the TwBs, the boojums are now located at the ends of the major axis of the spheroid and the director twists in the same helical pathway from the spherical case. The attraction of the boojums in the RSS morphology occurs in the region with higher curvature. Consequently, the surface-induced morphologies are stable at lower temperatures. For instance, we show how the RSS morphology that is observed for $\varphi = 1$ turns into a well defined BPI for $\varphi = 1.1$ under the same conditions of τ and N.

The destabilization of the droplet morphologies is more evident as the anchoring is weakened, Fig. 6B. For low chirality, the bipolar phase becomes a uniform phase that is oriented along the major axis, while the TwBs becomes a TC. The RSS structure is not observed and the τ-Ch phase appears, where the trefoil pattern covers the surface with parallel orientation domains that avoid the high-curvature regions. This phase is destabilized as φ increases, and is replaced by a BPI.

An interesting effect is observed in the region where the BPII is usually found. As the droplet is stretched, a combination of the two BP defect structures is generated. The tetrahedral structure of the BPII defects is kept and stretched, and long disclination lines, characteristic of a BPI, cross the lattice along the newly opened spaces. The BP hexagonal pattern on the surface is not altered. We call these phases hybridized BP (hBP). They are shown using red, blue, and green colors for the defect morphologies in the figure.

An oblate is formed by pressing down on two opposite points of the droplet. The oblate phase diagrams are shown in Fig. 7 for $0.5 < \varphi < 0.9$. Under strong anchoring conditions, Fig. 7A, the only destabilization occurs in the transition from TwBs to
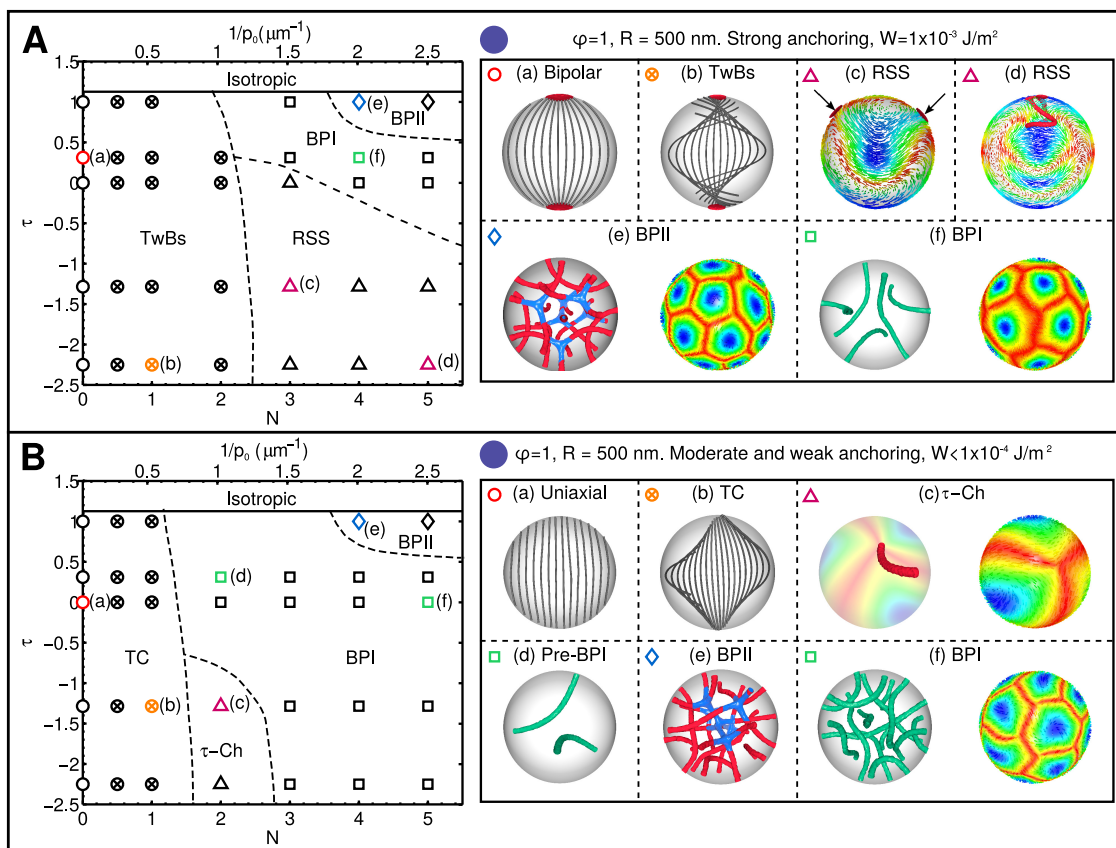
Fig. 5 Phase diagrams with the corresponding stable morphologies for a chiral LC **droplet** under (A) strong surface anchoring $W = 1 \times 10^{-3} J/m^2$ and (B) moderate anchoring $W = 1 \times 10^{-4} J/m^2$ conditions. On the left we present the phase diagrams in terms of $\tau = 9(3-U)/U$ and N, and representative configurations are shown on the right. Bipolar, Twisted Bipolar (TwBs), Radial Spherical Structure (RSS), Blue Phase II (BPII), and Blue Phase I (BPI) are shown for strong anchoring and Uniaxial, Twisted Cylinder (TC), τ–Cholesteric (τ-Ch), Blue Phase II (BPII) and Blue Phase I (BPI) for moderate anchoring. Iso-surfaces of the scalar order parameter are shown in red, blue and green. Streamlines of the director field are represented by the gray lines. The surface colormaps indicate the orientation of the LC molecules with respect to the surface: red for parallel and blue for perpendicular alignment.
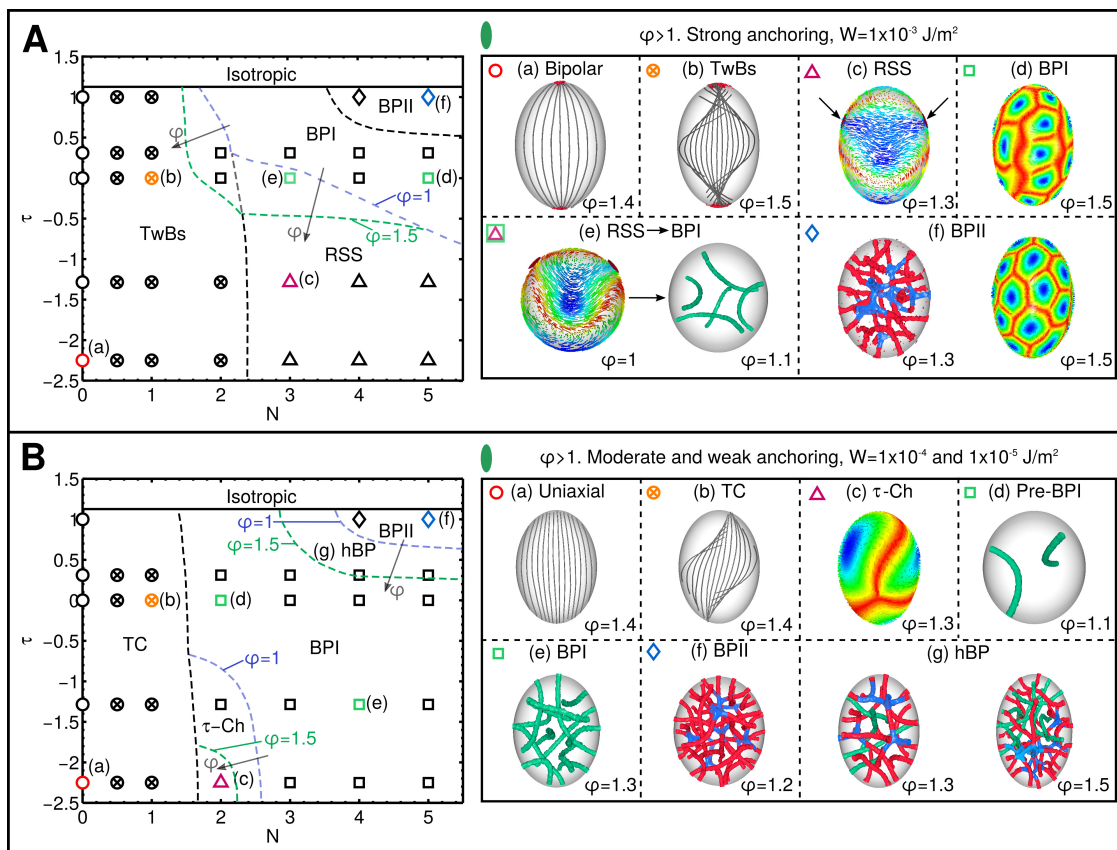
Fig. 6 Phase diagrams with the corresponding stable morphologies for a chiral LC **prolate** under (A) strong surface anchoring $W = 1 \times 10^{-3} J/m^2$ and (B) moderate anchoring $W = 1 \times 10^{-4} J/m^2$ conditions. On the left we present the phase diagrams in terms of τ vs. N, while representative configurations are shown on the right. Shaded regions correspond to changes in the phase diagram with respect to $\varphi = 1$. Bipolar, Twisted Bipolar (TwBs), Radial Spherical Structure (RSS), Blue Phase II (BPII), and Blue Phase I (BPI) are shown for strong anchoring and Uniaxial, Twisted Cylinder (TC), τ–Cholesteric (τ-Ch), Blue Phase II (BPII) and Blue Phase I (BPI) for moderate (low) anchoring. Iso-surfaces of the scalar order parameter are shown in red, blue and green. Streamlines of the director field are represented by the gray lines. The surface colormaps indicate the orientation of the LC molecules with respect to the surface: red for parallel and blue for perpendicular alignment.
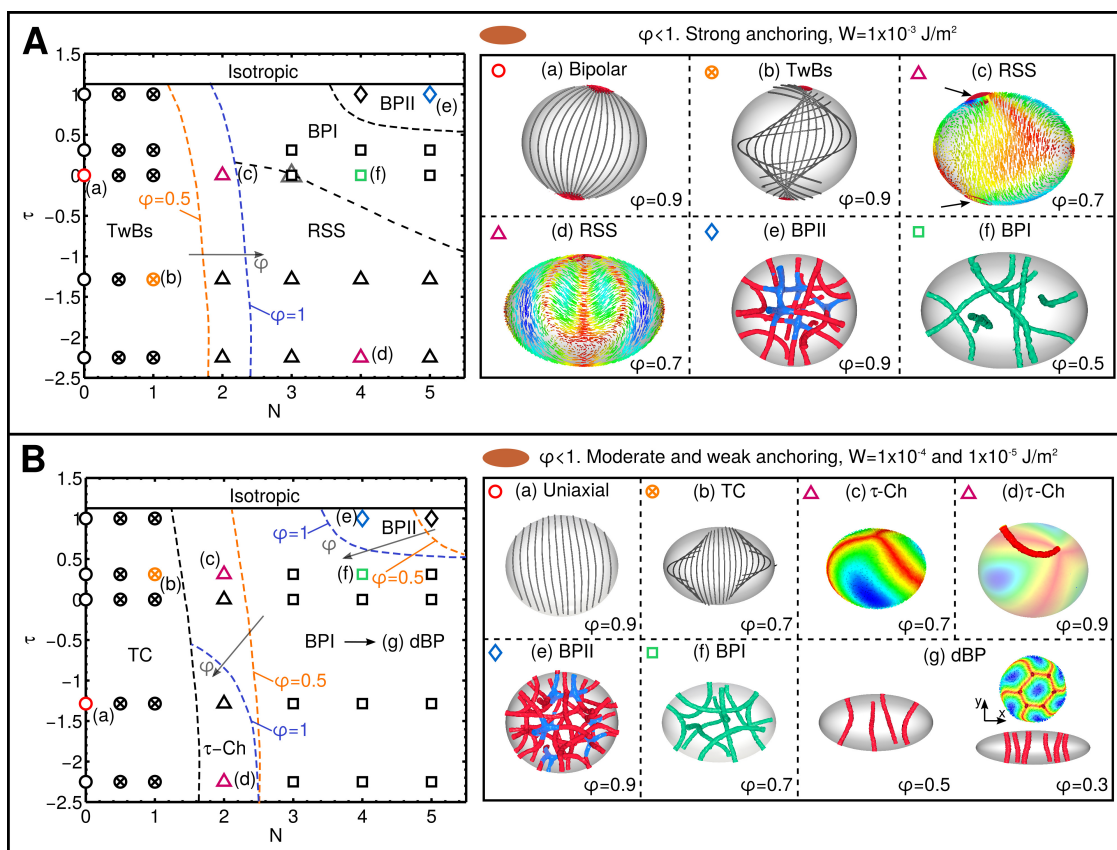
Fig. 7 Phase diagrams that summarize stable morphologies for a chiral LC **oblate** under (A) strong surface anchoring $W = 1 \times 10^{-3} J/m^2$ and (B) moderate anchoring $W = 1 \times 10^{-4} J/m^2$ conditions. On the left we present the phase diagrams τ vs. N, while on the right representative configurations are highlighted for completeness. Shaded regions correspond to changes in the phase diagram with respect to $\varphi = 1$. Bipolar, Twisted Bipolar (TwBs), Radial Spherical Structure (RSS), Blue Phase II (BPII), and Blue Phase I (BPI) are shown for strong anchoring and Uniaxial, Twisted Cylinder (TC), τ–Cholesteric (τ-Ch), Blue Phase II (BPII) and Blue Phase I (BPI) for moderate (low) anchoring. Iso-surfaces of the scalar order parameter are shown in red, blue and green. Streamlines of the director field are represented by the gray lines. The surface colormaps indicate the orientation of the LC molecules with respect to the surface: red for parallel and blue for perpendicular alignment.
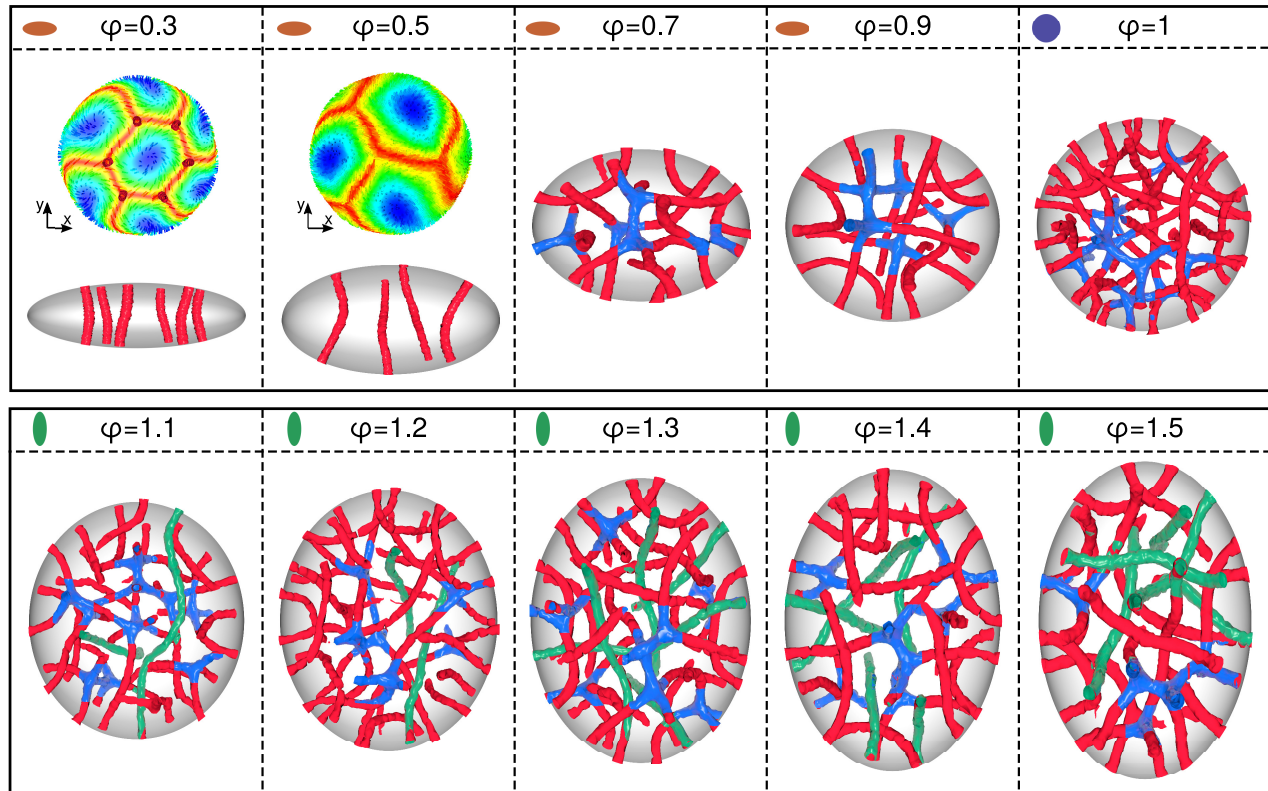
Fig. 8 Progression of blue phases as φ increases for high temperature and moderate anchoring conditions. Derived blue phases (dBP) are observed for oblates with $\varphi < 0.5$. Defect lines join and form BPII structures as the geometry resembles a droplet. For $\varphi > 1$ the hybridization of BPs occur. The defect structure is colored in red, tetrahedral joints are highlighted in blue and defect lines typical of BPI are colored in green. Surface patterns are colored according to the director orientation with respect to the imposed boundary conditions, red signifies parallel and blue is perpendicular alignment. For clarity we only show a section of the bulk defect structure.

RSS, when φ is lowered. The bipolar and TwBS phases show the two surface boojums aligned with the minor axis of the geometry when $\varphi < 0.7$. If the sphericity is not strongly altered, the boojums are displaced from the z-axis towards the region with higher curvature and are not necessarily antipodal. This predisposes the TwBS to form the RSS. The BPs are stable in the same temperature and chirality intervals than in the spherical droplet.

For moderate and weak anchoring conditions, Fig. 7B, the τ-Ch phase is stabilized as a precursor of the BPI. The stable region for the BPII moves to higher chirality as φ decreases. The original BP morphologies are deformed to create defect structures without an identifiable symmetry; we call these new phases derived BP (dBP). The disclination lines cross through the oblate and touch the surface. They form hexagonal patterns of λ disclinations similar to the half-skyrmion structures observed in nanochannels.

3.3 Additional discussion on chiral tactoids

The are three particular phenomena that merit additional discussion: (i) the progression of BP morphologies as φ is modified from 0.3 to 1.5, (ii) the specifics of the Twisted cylinder structure, and (iii) the multiple orientations of the cholesteric phases.

As can be seen in the phase diagrams, Figs. 5–7, the regions of stability are affected by the confining geometry. However, simulations show that cholesteric morphologies are not modified drastically by geometrical frustration. At the other end of the chirality spectrum, we find an intriguing behavior at high temperatures. We consider tactoids under moderate and low anchoring with $N = 4, 5$ and $\tau \in [0.5, 1]$. In Figure 8, we delineate how the BP changes from the dBP to the hBP as φ is increased from 0.3 to 1.5. For oblates ($\varphi < 1$), the formation of a BP is hindered by the narrow space along the z-direction. This causes an interruption in the symmetry and periodicity of the defect network, which makes it impossible to distinguish between BPII and BPI. The defects are tubes that touch the surface of the oblate and, together, they form structures similar to those found in nanochannels, namely 2D skyrmions shown in [22]. As the oblate loses its eccentricity ($\varphi \to 0.7$), the defects join and form a precursor for BPII which later develops in a spherical geometry (droplet, $\varphi = 1$).

As the droplet is stretched ($\varphi > 1$), we observe a hybridization of the blue phases. The defect structure exhibits tetrahedral junctures typical of BPII (in blue) and long disconnected defect lines characteristic of BPI (in green). As the geometry starts resembling a spindle, more BPI-like disclination lines appear, thus obtaining a heavily populated bulk. When defects reach the boundary of the prolate, they imprint the hexagonal pattern of surface defects characteristic of confined BPs. In practice, the heavily populated bulk implies a change in the lattice parameter, which affects the color of the sample that ensues from Bragg's law. Simulations for prolate systems that start from the ansatz for BPI and BPII show higher energies than the Hybrid Blue Phase identified here in MC simulations. However, it has only been possible to observe this new morphology by starting from an initial random orientation. This suggests that hBPs are stable but rare.

Although cholesteric morphologies do not undergo severe transformations, we would like to expand on the nature of the
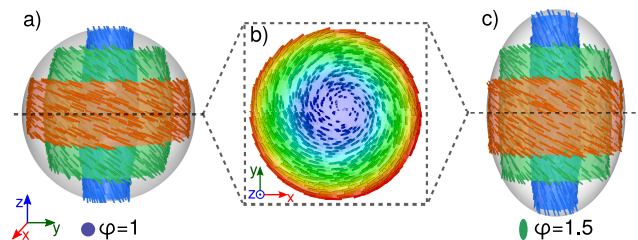

Fig. 9 Twisted cylinder structure in (a) a droplet ($\varphi = 1$) and (c) a prolate (φ) with $N = 1$ and $W = 1 \times 10^{-4} J/m^2$. Three concentric cylindrical shells indicating different orientations of the director field. (b) Cross section view of the director field at $z = 0$. The color map indicates the molecular orientation relative to the z-axis: blue is parallel and red is perpendicular.

Twisted cylinder structure. The TC is stable in all geometries for low chiralities and under moderate to weak surface anchoring. This phase is a derivative of the TwBs when the director field is virtually unbounded. Notice that for both phases, TwBs and TC, the director follows a helical trajectory. However, the crucial difference lies in the presence of boojums. From these features, the TC is better described as consisting of concentric cylindrical shells with unique orientations of the director with respect to the major axis of the geometry. The TC is shown in Fig. 9 for a droplet and a prolate, illustrating how the cylindrical shells are stretched along the z-direction as φ increases. A cross-sectional view of the morphology shows how the outer shell follows the surface alignment, while the director twists gradually until it is parallel to the z-axis at the core of the geometry.

For systems with $\varphi \neq 1$, the cholesteric axis may adopt a tilt without a particular preferred angle. We discovered this behavior by realizing that out of multiple simulations, all started from random isotropic phases, the final cholesteric morphology was oriented in different angles with respect to the major axis.

To expand and explain this behavior, we studied systems with two chiralities $N = 0.5, 1$ and four different aspect ratios, $\varphi = 0.5, 1.1, 1.3, 1.5$. We used two different initial configurations: uniaxial and TC, both oriented at an angle θ with respect to the z-axis. Figure 10 shows the total free energy as a function of θ for a prolate with $\varphi = 1.5$ for $N = 0.5$ and 1. This free energy plot is representative of the other geometries. Note that the total free energy is practically independent of the orientation of the cholesteric. Figure 10 also includes the cholesteric morphologies, and shows surface orientation contours and the director field inside the prolate. The only energetic resistance to reorientation of the cholesteric along a particular direction is the surface free energy; however, the penalties from $\theta = 0$ to $\pi/2$ are of order $200 \, k_B T$, which can be neglected given the magnitude of the elastic free energy. Although there is no difference from the energetic point of view, there is a distortion of the TC as the cholesteric aligns with the minor axis of the geometry. This is evidenced by the torsion of the region parallel to the surface (red color) of the prolate as θ approaches $\pi/2$, similar to a lemniscate. These patterns of the surface contours are typical of a cholesteric phase as reported in [57]. On the other hand, for $\theta = 0$, the parallel regions form a perfect ring along the equator of the geometry.
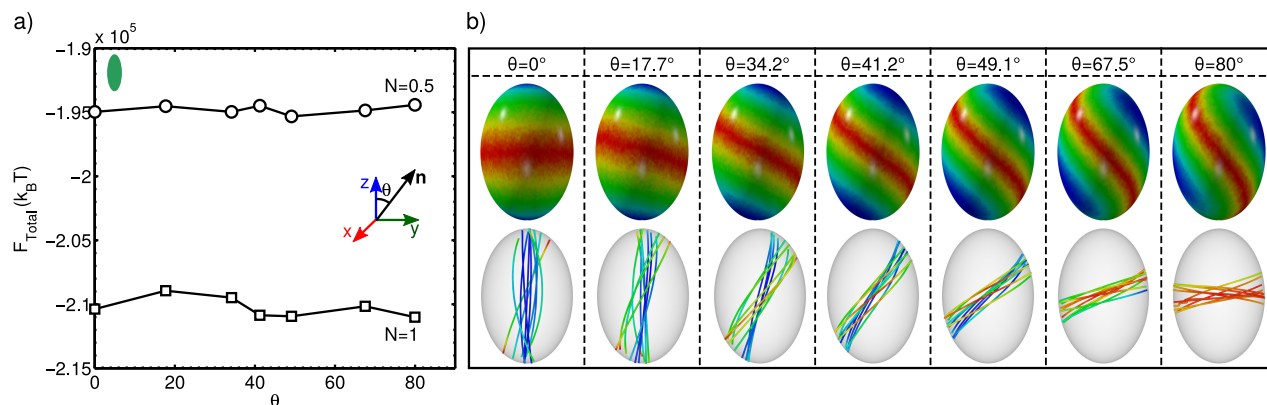
Fig. 10 Rotated TC in a prolate. (a) Total free energy versus inclination of the cholesteric rotation axis for $N = 0.5$ and $N = 1$ on a prolate ($\varphi = 1.5$) with moderate anchoring $W = 1 \times 10^{-4} J/m^2$. (b) Final configurations of tilted cholesterics at an angle θ respect to the z-axis. The top row shows the orientation of the molecules respect to the surface, red indicates parallel orientation and blue is perpendicular. The bottom row shows streamlines of the director field in the bulk of the prolate.

4   Conclusions

A systematic study of chiral nematics in spheroids has been carried out by resorting to a continuum description of the free energy. Simulations were implemented by minimizing the free energy through a theoretically informed Monte Carlo relaxation and a finite element discretization. The corresponding phase diagrams were determined in terms of temperature and chirality for three families of spheroids under strong, moderate and low anchoring conditions. The droplet phase diagram was consistent with those reported in the literature. As the anchoring is weakened, some phases transform into precursors to the BPs in the intermediate chirality regime, a feature that had not been appreciated in the past.

Geometric frustration helps stabilize and engendere new BP-like morphologies. The main consequence on changing the geometry is the widening or narrowing of some regions in the phase diagram. The high curvature on the spheroid becomes a region where surface defects are most stable, and facilitates the formation of structures like the RSS. The constriction in one dimension hinders the formation of symmetric defect networks, and lead to structures similar to those reported for BPs confined in nanochannels. As the spheroid takes a more spherical shape, the truncated BP transforms into a BPII. In the prolate shape, the bulk is highly populated by defects typical of BPI. The hybridization of both BPs provides a new region that has a distinct optical response, and serves to stabilize the BPs over wider ranges of temperature.

Conflicts of interest

There are no conflicts to declare.

Acknowledgements

Notes and references

1 E. Dubois-violette and B. Pansu, *Molecular Crystals and Liquid Crystals Incorporating Nonlinear Optics*, 1988, **165**, 151–182.
2 H. Kikuchi, M. Yokota, Y. Hisakado, H. Yang and T. Kajiyama, *Nature Materials*, 2002, **1**, 64–8.
3 J. M. Brake, M. K. Daschner, Y. Y. Luk and N. L. Abbott, *Science*, 2003, **302**, 2094–7.
4 I. H. Lin, D. S. Miller, P. J. Bertics, C. J. Murphy, J. J. de Pablo and N. L. Abbott, *Science*, 2011, **332**, 1297–300.
5 M. Sadati, A. I. Apik, J. C. Armas-Pérez, J. A. Martínez-González, J. P. Hernández-Ortiz, N. L. Abbott and J. J. de Pablo, *Advanced Functional Materials*, 2015, **25**, 6050–6060.
6 P. Etchegoin, *Physical Review E*, 2000, **62**, 1435–1437.
7 W. Cao, A. Muñoz, P. Palffy-Muhoray and B. Taheri, *Nature Materials*, 2002, **1**, 111–113.
8 T.-H. Lin, Y. Li, C.-T. Wang, H.-C. Jau, C.-W. Chen, C.-C. Li, H. K. Bisoyi, T. J. Bunning and Q. Li, *Advanced Materials*, 2013, **25**, 5050–5054.
9 I. Musevic, *Philosophical transactions. Series A, Mathematical, physical, and engineering sciences*, 2013, **371**, 20120266.
10 O. Henrich, K. Stratford, D. Marenduzzo, P. V. Coveney and M. E. Cates, *Journal of Physics: Condensed Matter*, 2012, **24**, 284127.
11 A. Tiribocchi, M. E. Cates, G. Gonnella, D. Marenduzzo and E. Orlandini, *Soft Matter*, 2013, **9**, 4831.
12 F. Castles, S. M. Morris, E. M. Terentjev and H. J. Coles, *Physical Review Letters*, 2010, **104**, 157801.
13 M. Ravnik, *Liquid Crystals Today*, 2011, **20**, 77–84.
14 I. Dierking, W. Blenkhorn, E. Credland, W. Drake, R. Kociuruba, B. Kayser and T. Michael, *Soft Matter*, 2012, **8**, 4355.
15 J. I. Fukuda, *Physical Review E*, 2012, **85**, 020701.

16 I. Gvozdovskyy, *Liquid Crystals*, 2015, **42**, 1391–1404.

17 M. D. A. Rahman, S. Mohd Said and S. Balamurugan, *Science and Technology of Advanced Materials*, 2015, **16**, 033501.

18 C.-L. Wei, T.-C. Chen, P. Raghunath, M.-C. Lin and H.-C. Lin, *RSC Advances*, 2015, **5**, 4615–4622.

19 A. Singh, P. Malik and D. Jayoti, *International Journal of Modern Physics B*, 2016, **30**, 1650011.

20 R. D. Kamien and J. V. Selinger, *Journal of Physics: Condensed Matter*, 2001, **13**, R1–R22.

21 J. I. Fukuda and S. Žumer, *Physical Review Letters*, 2010, **104**, 1–4.

22 J. I. Fukuda and S. Žumer, *Nature Communications*, 2011, **2**, 246.

23 M. Melle, M. Theile, C. K. Hall and M. Schoen, *International Journal of Molecular Sciences*, 2013, **14**, 17584–17607.

24 P. J. Ackerman, T. Boyle and I. I. Smalyukh, *Nature Communications*, 2017, **8**, 673.

25 J. A. Martínez-González, X. Li, M. Sadati, Y. Zhou, R. Zhang, P. F. Nealey and J. J. de Pablo, *Nature Communications*, 2017, **8**, year.

26 X. Li, J. A. Martínez-González, J. P. Hernández-Ortiz, A. Ramírez-Hernández, Y. Zhou, M. Sadati, R. Zhang, P. F. Nealey and J. J. de Pablo, *Proceedings of the National Academy of Sciences*, 2017, **114**, 10011–10016.

27 X. Li, J. A. Martínez-González, K. Park, C. Yu, Y. Zhou, J. J. de Pablo and P. F. Nealey, *ACS Applied Materials & Interfaces*, 2019, **11**, 9487–9495.

28 J. Bajc, P. P. Crooker and S. Zumer, *Liquid Crystals Today*, 1997, **7**, 1–6.

29 F. Xu and P. Crooker, *Physical Review E*, 1997, **56**, 6853–6860.

30 D. Seč, T. Porenta, M. Ravnik and S. Žumer, *Soft Matter*, 2012, **8**, 11982.

31 E. Kemiklioglu and L.-c. Chien, *Applied Physics Express*, 2014, **7**, 091701.

32 D. Seč, S. Copar and S. Zumer, *Nature communications*, 2014, **5**, 3057.

33 J. A. Martínez-González, Y. Zhou, M. Rahimi, E. Bukusoglu, N. L. Abbott and J. J. de Pablo, *Proceedings of the National Academy of Sciences*, 2015, **112**, 13195–13200.

34 M. B. Pandey, P. J. Ackerman, A. Burkart, T. Porenta, S. Žumer and I. Smalyukh, *Physical Review E*, 2015, **91**, 012501.

35 T. Orlova, S. J. Aßhoff, T. Yamaguchi, N. Katsonis and E. Brasselet, *Nature Communications*, 2015, **6**, 7603.

36 A. Dupuis, D. Marenduzzo and J. M. Yeomans, *Physical Review E*, 2005, **71**, 011703.

37 A. Tiribocchi, G. Gonnella, D. Marenduzzo and E. Orlandini, *Soft Matter*, 2011, **7**, 3295.

38 D. Vanzo, M. Ricci, R. Berardi and C. Zannoni, *Soft Matter*, 2012, **8**, 11790–11800.

39 a. V. Kaznacheev, M. M. Bogdanov and a. S. Sonin, *Journal of Experimental and Theoretical Physics*, 2003, **97**, 1159–1167.

40 L. Tortora and O. D. Lavrentovich, *Proceedings of the National Academy of Sciences of the United States of America*, 2011, **108**, 5163–5168.

41 Y.-K. Kim, S. V. Shiyanovskii and O. D. Lavrentovich, *Journal of Physics: Condensed Matter*, 2013, **25**, 404202.

42 C. Peng and O. D. Lavrentovich, *Soft Matter*, 2015, **11**, 7257–7263.

43 F. Castles, S. M. Morris, J. M. C. Hung, M. M. Qasim, A. D. Wright, S. Nosheen, S. S. Choi, B. I. Outram, S. J. Elston, C. Burgess, L. Hill, T. D. Wilkinson and H. J. Coles, *Nature Materials*, 2014, **13**, 817–821.

44 F. Castles, *Applied Physics Letters*, 2015, **107**, 101106.

45 P.-X. Wang and M. J. MacLachlan, *Philosophical Transactions of the Royal Society A: Mathematical, Physical and Engineering Sciences*, 2017, **376**, 20170042.

46 P.-X. Wang, W. Y. Hamad and M. J. MacLachlan, *Angewandte Chemie International Edition*, 2018, **57**, 3360–3365.

47 A. Beris and B. Edwards, *Thermodynamics of flowing systems: with internal microstructure*, Oxford Science Publications, Oxford, 1994.

48 M. J. Stephen and J. P. Straley, *Reviews of Modern Physics*, 1974, **46**, 617–704.

49 T. C. Lubensky, *Physical Review A*, 1970, **2**, 2497–2514.

50 A. Saupe, *The Journal of Chemical Physics*, 1981, **75**, 5118.

51 P. de Gennes and J. Prost, *The Physics of Liquid Crystals*, Oxford University Press, Oxford, 2nd edn, 1995.

52 M. Doi, *Journal of Polymer Science: Polymer Physics Edition*, 1981, **19**, 229–243.

53 C. W. Oseen, *Transactions of the Faraday Society*, 1933, **29**, 883–99.

54 F. C. Frank, *Discussions of the Faraday Society*, 1958, **25**, 19–28.

55 H. Mori, E. C. Gartland, J. R. Kelly and P. J. Bos, *Japanese Journal of Applied Physics, Part 1: Regular Papers and Short Notes and Review Papers*, 1999, **38**, 135–146.

56 J.-B. Fournier and P. Galatola, *Europhysics Letters*, 2006, **72**, 403–409.

57 J. C. Armas-Pérez, J. P. Hernández-Ortiz and J. J. de Pablo, *The Journal of Chemical Physics*, 2015, **143**, 243157.

58 J. C. Armas-Pérez, A. Londoño-Hurtado, O. Guzmán, J. P. Hernández-Ortiz and J. J. de Pablo, *The Journal of Chemical Physics*, 2015, **143**, 044107.

59 S. Villada-Gil, V. Palacio-Betancur, J. C. Armas-Pérez, J. J. de Pablo and J. P. Hernández-Ortiz, *Journal of Physics: Condensed Matter*, 2019, **31**, 175101.

60 P. Kaiser, W. Wiese and S. Hess, *Journal of Non-Equilibrium Thermodynamics*, 1992, **17**, 153–170.

61 Sandia National Laboratories, *Cubit Version 14.1*, 2014.

62 B. S. Kirk, J. W. Peterson, R. H. Stogner and G. F. Carey, *Engineering with Computers*, 2006, **22**, 237–254.

63 X. Li, J. C. Armas-Perez, J. A. Martinez-Gonzalez, X. Liu, H. Xie, C. Bishop, J. P. Hernandez-Ortiz, R. Zhang, J. J. de Pablo and P. F. Nealey, *Soft Matter*, 2016, **12**, 8595–8605.

64 J. C. Armas-Pérez, X. Li, J. A. Martínez-González, C. Smith, J. P. Hernández-Ortiz, P. F. Nealey and J. J. de Pablo, *Langmuir*, 2017, **33**, 12516–12524.

65 A. Londoño-Hurtado, J. C. Armas-Pérez, J. P. Hernández-Ortiz   and J. J. de Pablo, *Soft Matter*, 2015, **11**, 5067–5076.

Cuboidal liquid crystal phases under multiaxial geometrical frustration

V. Palacio–Betancur, J.C. Armas–Pérez, S. Villada–Gil,
N.L. Abbott, J.P. Hernández–Ortiz and J.J. de Pablo

Oblate   Sphere   Prolate
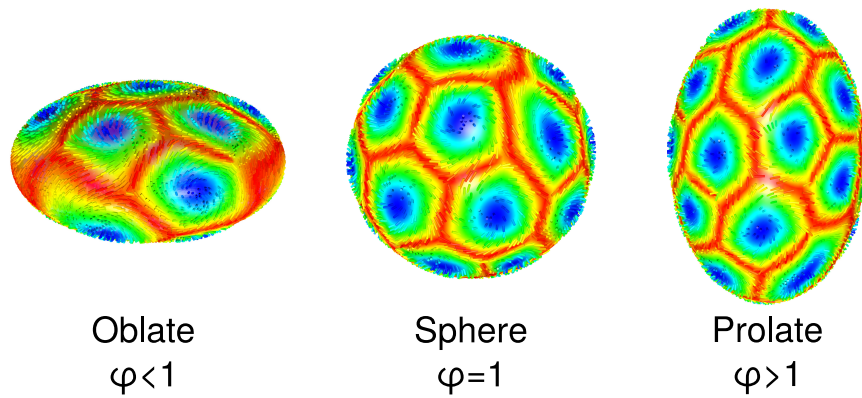$\varphi < 1$ $\varphi = 1$ $\varphi > 1$

Figure 1: Chiral LCs confined in spheroids exhibit new families of morphologies as a result of geometrical frustration.

1